Boosting the CO_2 electroreduction performance of $La_{2-x}Ag_xCuO_{4-\delta}$ perovskites via A-site substitution mechanism

Gang Dong [a], Guo Wang [b], Jiarun Cheng [a], Meng Li [a], Zhifu Liang [c], Dongsheng Geng [c,*], Weiqiang Tang [d,*]

[a] *School of Materials Science and Engineering, University of Science and Technology Beijing, Beijing 100083, China*
[b] *School of Nuclear Science and Engineering, North China Electric Power University, Beijing 102206, China*
[c] *School of Chemistry and Materials Science, Nanjing University of Information Science & Technology, Nanjing 210044, China*
[d] *State Key Laboratory of Chemical Engineering and School of Chemical Engineering, East China University of Science and Technology, Shanghai 200237, China*

ARTICLE INFO

ABSTRACT

The electrochemical CO_2 reduction reaction (CO_2RR) has been widely recognized as a promising approach to achieve the carbon cycle balance in human society. However, potent electrocatalysts are required to achieve the selective conversion of CO_2 to high value-added chemical products. Here, we reported a Ruddlesden-Popper layered perovskite catalyst, namely $La_{2-x}Ag_xCuO_{4-\delta}$, which exhibits enhanced activity and selectivity towards CO_2RR by tuning the A-site cations with Ag doping. Combinatorial characterizations and theoretical calculation reveal the partial replacement of Ag^+ on the A-site of La_2CuO_4 can tune the electronic structure of Cu^{2+} ions of the B site, improving the adsorption/activation of crucial reaction intermediates. Importantly, Ag doping constructs oxygen vacancies, which shifts the reaction pathways from the two-electron transfer reduction to the multi-electron/proton transfer reduction, thereby promoting the formation of multi-carbon products. Taken together, these findings offer fresh insights for the strategic development of efficient perovskite electrocatalysts for CO_2RR.

1. Introduction

Carbon dioxide (CO_2) emissions, the primary driver of the greenhouse effect, have a serious impact on the global climate, presenting an imminent and potentially irreversible peril to society [1–4]. Leveraging green energy for electrocatalytic conversion of CO_2 into high-value chemical products offers a potent strategy to curb CO_2 buildup, sustain the carbon cycle, and tackle pressing environmental challenges and energy shortages [5–8]. The electrocatalytic CO_2 reduction reaction (CO_2RR) primarily involves the following fundamental steps: (i) Adsorption and activation of CO_2 on the active site form intermediate species (e.g., $*CO_2^-$, $*HCO_2^-$, $*$ denotes surface adsorbed species); (ii) C−O bond of the intermediate species undergoes dissociation, involving complex proton-coupled-electron multiple transfer process; (iii) The reduced products are desorbed from the active site [8–12]. With regard to the steps above, the chemical activation of CO_2 has become a crucial factor in the development of efficient CO_2RR [13]. However, the CO_2RR suffers from sluggish kinetics and poor selectivity, primarily attributed to the inevitably competitive hydrogen evolution reaction (HER) and

high overpotentials, which severely hinders the efficient production of highly value-added multi-carbon (C_2, e.g., C_2H_5OH, C_2H_4) products [14–16]. Accordingly, efforts aimed at reducing the activation energy barrier of CO_2 are the key to achieving immense significance in advancing the field of CO_2RR technology.

Among various developed electrocatalysts, transition metal oxides (such as ZnO, Cu_2O) have garnered notable interest in the field of electrocatalysis due to their favorable catalytic activity, moderate cost, and abundant reserves [17–19]. Most recently, several studies have shown that the catalytic activities of oxide materials are not only influenced by the intrinsic activity of the metal sites but also by oxygen vacancies [20–22]. Through oxygen vacancy engineering, it is possible to effectively adjust the electronic structure, charge transfer, and adsorption of reaction intermediates, promoting the activation and dissociation of CO_2 [23,24]. As well known, a higher concentration of oxygen vacancies in oxide materials results in stronger metal-oxygen covalent bonds [25]. The binding of metal cations with neighboring oxygen vacancies serves as unsaturated active centers that can weaken C═O bonds, making CO_2 molecules more prone to participate in

---

* Corresponding authors.
E-mail addresses: dgeng@nuist.edu.cn (D. Geng), wqtang@ecust.edu.cn (W. Tang).

reactions. This reduces the reaction energy barriers and facilitates the easier reduction of CO_2 molecules into desired hydrocarbon compounds. As a result, the catalytic activity of oxide materials in CO_2RR is enhanced. This increased activity leads to improved Faradaic efficiency (FE) for C_2 products. The presence of oxygen vacancies significantly enhances the activation of CO_2 and promoting the selective formation of desired products during the CO_2RR process. For instance, Geng et al. conducted density functional theory (DFT) calculations to confirm that the introduction of oxygen vacancies increases the charge density of ZnO near the valence band, thereby enhancing the activation of CO_2 [19]. However, oxygen vacancies are typically located within the catalyst's interior rather than on the surface, which may limit their participation in the catalytic reaction effectively [26]. Also, complex microstructures such as interfaces and capping agents may have detrimental effects on identifying the role of oxygen vacancies in the CO_2RR process [27]. Therefore, the intrinsic effect of oxygen vacancies on CO_2RR activities cannot be comprehensively understood yet. To gain a deeper insight into the atomic-level relationship between oxygen vacancies and the characteristics of CO_2RR, it is crucial to combine simplified catalyst models with oxygen vacancies in real catalytic systems.

Compared to other metal oxides, the Ruddlesden-Popper La_2CuO_4 (RP LCO) perovskite oxide possesses easily tunable electronic properties, allowing certain metal cations to exist in unusual or mixed valence states, thereby creating oxygen vacancies. Moreover, RP LCO perovskite oxide exhibits the characteristic of controllable oxygen vacancy concentration [28–31]. For instance, Zhu et al. demonstrated that cation vacancies can induce the generation of oxygen vacancies in La_2CuO_4. Among these, $La_{1.9}CuO_{4-\delta}$ exhibited the highest CO_2RR activity and the best selectivity towards C_{2+} products, achieving the FE of 41.5% [20]. Chen et al. have confirmed that the interfacial Cu atoms in Cu/La_2CuO_4 are related to its excellent activity in CO_2 methanation [32]. Although breakthroughs have been made in this field, the CO_2RR performance of perovskite-type oxides is still far from meeting the needs of practical industrial production. Generally, single-carbon (C_1) products (e.g., CO, CH_4) are mainly formed in most CO_2RR processes using perovskite-type oxides as electrocatalysts, while value-added hydrocarbons C_2 products are rarely obtained. The low conductivity and catalytic activity of RP LCO hinder further improvement in electrocatalytic performance. These limitations can be addressed through various approaches. On one hand, the synthesis conditions can be modified to enhance the properties of RP LCO. Methods such as sol-gel synthesis, co-precipitation, or solid-state reactions can be employed to optimize the material's structure and composition. On the other hand, the conductivity of RP LCO can be improved by doping with highly active metal cations like Ag. The introduction of these dopants enhances the conductivity of the material, facilitating efficient charge transport during electrocatalytic reactions. Additionally, the concentration of oxygen vacancies can be precisely controlled through doping, leading to enhanced catalytic activity [33]. During the CO_2RR, La elements play a crucial role in maintaining the catalyst's crystal structure, ensuring that irreversible structural changes do not occur under reaction conditions. Additionally, La elements possess the ability to adjust the electronic structure of the catalyst, influencing electron transfer properties, thereby contributing to improved efficiency in CO_2 electrocatalysis. Cu elements are generally considered one of the active centers in carbon dioxide electrocatalysis, providing sites for reactant adsorption and participating in the formation of reaction intermediates. Cu can catalyze the reduction of CO_2, converting it into other valuable compounds, such as ethanol and ethylene. Furthermore, the ionic radii of Ag and La elements are close, allowing Ag^+ to substitute for La^{3+}, thereby creating oxygen vacancies. Simultaneously, during the reaction, this can also provide a higher local concentration of CO at the catalysts, thereby enhancing the electrocatalytic activity of CO_2RR. Therefore, La and Cu elements play critical roles in CO_2 electrocatalysis by maintaining the structural stability of the catalyst, adjusting the electronic structure, providing reaction sites, and with the auxiliary effect of Ag, collectively promoting efficient CO_2RR

reactions. By combining both the optimization of synthesis conditions and doping strategies, it is possible to tailor the characteristics of RP LCO, achieving high catalytic activity and improved electrocatalytic performance. We propose that by adjusting the A sites of perovskite oxides, it is possible to tailor the adsorption and desorption properties of intermediates. This, in turn, could help in lowering the thermodynamic barriers for CO_2RR catalysis. These approaches offer opportunities to overcome the inherent limitations of RP LCO and unlock its full potential as an effective electrocatalyst.

Here, we report a simple and reliable method to improve the CO_2RR performance by substituting the A-site cations in RP La_2CuO_4 catalysts with Ag^+ ions. A series of $La_{2-x}Ag_xCuO_{4-\delta}$ ($L_{2-x}A_xCO$, $x = 0 \sim 0.5$, where x represents the molar ratio) were synthesized by the sol-gel technique. As anticipated, Ag^+ partially substituted La^{3+} at the A-site cation within La_2CuO_4. Within such a system framework, according to the electroneutrality principle, the substitution of A-site cations can alter the crystal structure of perovskite catalysts, leading to non-conservation of total charges and the generation of suitable oxygen vacancies [34–36]. The investigation delved into the interplay among Ag doping concentration, oxygen vacancy formation, and the change of active sites. Specifically, the doping of Ag introduces a certain amount of oxygen vacancies into the $L_{2-x}A_xCO$ catalysts, which promotes the electron transfer, shifts the D-band center to be closer to the Fermi level, and enhances the adsorption of intermediate products, and provides abundant active sites for CO_2 electrocatalysis. When evaluated as a catalyst toward CO_2RR, the $L_{1.8}A_{0.2}CO$ perovskite catalyst exhibited the highest activity and selectivity for C_2 products with greatly improved stability. A high FE of 86.4% with a partial current density of 22.7 mA cm^{-2} for C_2 product is achieved over this $La_{1.8}Ag_{0.2}CO$ perovskite catalyst at -1.1 V vs RHE, which is comparable to or better than most reported Cu-based oxides. Both experiments and theoretical calculations suggested that the cation substitution at the A site cations induced the interesting physicochemical properties, which can not only regulate the adsorption and activation of important reactive species, but also tune electron/proton transfer to optimize CO_2RR performance. This work provides an effective strategy for manipulating C_2 products in CO_2RR by governing oxygen vacancies of perovskite catalysts. This research offers valuable insights into the dynamics of oxygen vacancies during electrochemical reactions and the interaction mechanism between these vacancies and metal sites. Additionally, it introduces novel viewpoints for the strategic design of high-performance perovskite oxidation catalysts.

2. Experimental section

2.1. Chemicals and materials

Lanthanum(III) nitrate hexahydrate ($La(NO_3)_3 \cdot 6H_2O$, 99%), copper (II) nitrate trihydrate ($Cu(NO_3)_2 \cdot 3H_2O$, 99%), silver nitrate ($AgNO_3$, 99.8%), potassium bicarbonate ($KHCO_3$, 99.5%), Citric acid monohydrate ($C_6H_8O_7 \cdot H_2O$, 99.8%), ethanol (AR), ethylene glycol (AR), isopropanol (AR), Nafion solution (5 wt%), Nafion117 membrane, experimental water is deionized water. All chemicals are directly put into use without further purification.

2.2. Synthesis of $La_{2-x}Ag_xCuO_{4-\delta}$ catalysts

In order to prepare the $L_{2-x}A_xCO$ samples, the citrate-based sol-gel route was adopted. By dissolving nitrate reagent, stoichiometric amounts of $La(NO_3)_3 \cdot 6H_2O$, $Cu(NO_3)_2 \cdot 3H_2O$ and $AgNO_3$ were dissolved in deionized water to obtain a mixed solution. Then, the appropriate amount of citric acid (The molar ratio of citric acid to all metal cations was set to 4:1) and 15 ml of ethylene glycol were introduced into the as-prepared mixture containing metal precursor solution. The as-prepared $L_{2-x}A_xCO$ precursor solution was constantly stirred and heated at 80 ℃ using magnetic stirrer until becoming the brown wet gel. The obtained

wet gel was subsequently heated in the oven at 180 ℃ for 12 h until the gel was decomposed and produced a solid precursor. Finally, in an agate mortar, the solid precursor was ground and calcined at 950 ℃ for 10 h with the heating and cooling rate of 5 ℃ min^{-1} to obtain the L$_{2-x}$A$_x$CO samples.

3. Results and discussions

All materials were synthesized using a modified sol-gel method [37, 38]. The crystal structure of La$_2$CuO$_4$ is illustrated in Fig. 1a, where the CuO$_6$ octahedron is regularly positioned within the structure and the La atom is inserted into the octahedral space. The crystal structures of
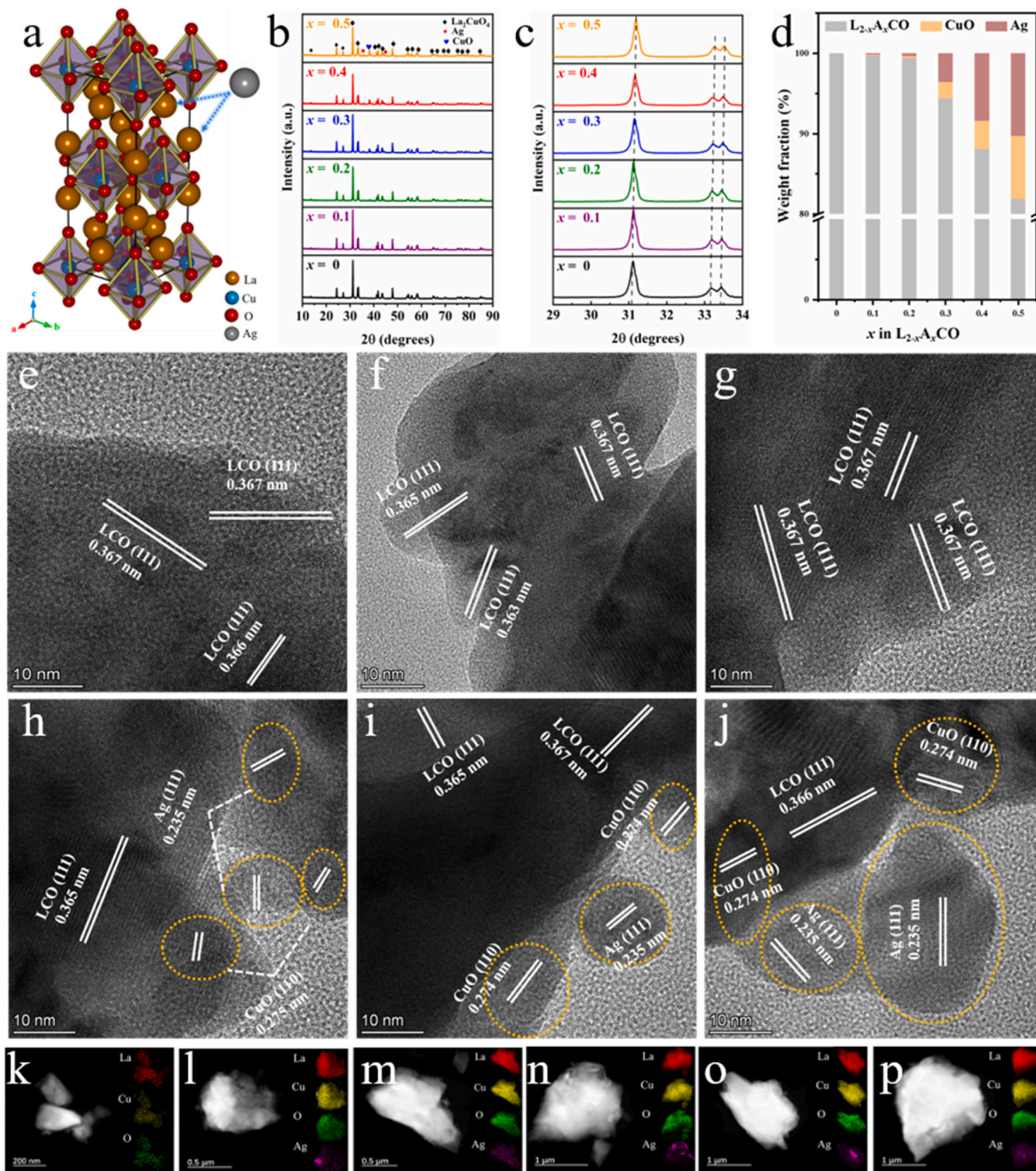

Fig. 1. (a) Structural scheme of Ruddlesden–Popper series of layered perovskite oxides. (b) XRD diffraction pattern of L$_{2-x}$A$_x$CO samples. (c) Detailed view of 2θ from 29.0 to 34.0°. (d) Weight fractions of the L$_{2-x}$A$_x$CO, Ag and CuO phases obtained from Rietveld refinement of XRD data. (e-j) HRTEM image of the L$_{2-x}$A$_x$CO samples: (e) L$_2$CO, (f) L$_{1.9}$A$_{0.1}$CO, (g) L$_{1.8}$A$_{0.2}$CO, (h) L$_{1.7}$A$_{0.3}$CO, (i) L$_{1.6}$A$_{0.4}$CO and (j) L$_{1.5}$A$_{0.5}$CO. (k-p) EDS mapping of the L$_{2-x}$A$_x$CO samples: (k) L$_2$CO, (l) L$_{1.9}$A$_{0.1}$CO, (m) L$_{1.8}$A$_{0.2}$CO, (n) L$_{1.7}$A$_{0.3}$CO, (o) L$_{1.6}$A$_{0.4}$CO and (p) L$_{1.5}$A$_{0.5}$CO.

$L_{2-x}A_xCO$ have been confirmed through the analysis of X-ray powder diffraction (XRD) patterns, as presented in Fig. 1b. All examined catalysts exhibit a well-defined perovskite crystal structure and point accurately to a layered structure with a space group of *Fmmm* [32]. The sharp and intense diffraction peaks of $L_{2-x}A_xCO$ indicate its high purity, excellent crystallinity, and good perovskite structure. Inductively coupled plasma emission spectroscopy (ICP-OES) analysis confirmed that the chemical composition of all $L_{2-x}A_xCO$ catalysts is consistent with its nominal components. (Table S1). The addition of Ag to $L_{2-x}A_xCO$ results in the detection of a diffraction peak at 2θ of $38.12°$, which is attributed to the (111) reflection of cubic Ag. With the increase of Ag doping content, the corresponding diffraction peak intensity gradually increases. In fact, not all Ag could be atomically doped into the perovskite lattice during high-temperature sintering, leading to the in-situ precipitation of some silver ions to form metallic Ag [39]. Fig. 1b clearly shows a new diffraction peak appearing at about $35.5°$ in the XRD pattern with more Ag are introduced into the L_2CO parent catalyst, which can be assigned to the (110) reflections of monoclinic CuO (PDF#45–0937). This suggests that excessive Ag doping ($x > 0.2$) leads to the formation of a secondary phase, which becomes more pronounced with increasing Ag doping. Further investigation into the interrelation of crystal structure and composition of these samples with A-site substitution was conducted using Rietveld refinement analysis of the XRD data. (Fig. S1 and Table S2). The XRD patterns show that all catalysts contain CuO and Ag phases besides a RP phase of L_2CO (Fig. 1d). The weight fractions of CuO and Ag for each catalyst are as follows: $L_{1.9}A_{0.1}CO$ (0.1 wt% CuO and 0.2 wt% Ag), $L_{1.8}A_{0.2}CO$ (0.2 wt% CuO and 0.4 wt% Ag), $L_{1.7}A_{0.3}CO$ (2 wt% CuO and 3.6 wt% Ag), $L_{1.6}A_{0.4}CO$ (3.5 wt% CuO and 8.4 wt% Ag), and $L_{1.5}A_{0.5}CO$ (7.8 wt% CuO and 10.3 wt% Ag). The reason for this phenomenon is that under the condition of higher Ag concentrations, some Cu segregate into independent phases on the perovskite surface due to incomplete coordination. Consequently, it can be inferred that the upper limit for x in $L_{2-x}A_xCO$ should not surpass 0.2. There is a positive shift gradually for the selected enlarged main peaks (region of (113), (020) and (200) in Fig. 1c) of $L_{2-x}A_xCO$ with increasing Ag substitution. This result indicates that the partial substitution of larger La^{3+} ion (1.36 Å) with Ag^+ ion (1.28 Å) at the A site causes shrinkage of the perovskite unit cell [33,40]. With the increase of Ag content, the calculated unit cell volume of $L_{2-x}A_xCO$ gradually decreases, which is consistent with the XRD data, as displayed in Table S2.

The $L_{2-x}A_xCO$ catalysts were initially explored through scanning electron microscopy (SEM) and transmission electron microscopy (TEM) (Fig. S2). The average particle size of all catalysts is around 240 nm, and them remain nearly unchanged with an increase in Ag content. (Fig. S3). Therefore, Ag doping has no effect on the grain size of the catalyst. Fig. 1e-j show the high-resolution transmission electron microscopy (HRTEM) image of the catalysts, enabling the observation of their crystal structure and composition. The presence of the Ruddlesden-Popper phase was evident in all samples, as indicated by distinct crystal fringes exhibiting an interplanar spacing of approximately 0.367 nm. These spacings correspond to the (111) diffraction plane of perovskite La_2CuO_4 crystals. The observations indicated that no Ag-related lattice fringes were detected when the doping amount of Ag was less than or equal to 0.2. In Fig. 1k-p, the energy dispersive X-ray spectroscopy (EDS) mappings revealed a uniform distribution of La, Ag, Cu, and O, indicating successful incorporation of Ag into the perovskite lattice. With the increase of Ag content, when x exceeds 0.2, the sample exhibits Ag (111) diffraction planes, and lattice fringes have a *d*-spacings of approximately 0.235 nm. Furthermore, CuO (110) diffraction planes appear in the nano-domains of the sample with interplanar spacing of about 0.274 nm. Fig. 1h-j demonstrates that the in situ dissolution of Ag^+ was observed with high concentration of Ag doping [33]. Meanwhile, as the Ag doping ratio increases from 0.1 to 0.5 the isolated silver nanoparticles formed on the surface of the $L_{2-x}A_xCO$ catalysts gradually increase. It has been reported that these Ag nanoparticles can improve the electrical conductivity of the catalysts, facilitating the CO_2 reduction reaction and accelerating the formation of C_1 and C_2 products [41–43].

The X-ray photoelectron spectroscopy (XPS), iodometric titration, and electron paramagnetic resonance (EPR) were performed to elucidate the relationship between the Ag doping and oxygen vacancy in the $L_{2-x}A_xCO$ catalysts. The results of XPS reveal that these $L_{2-x}A_xCO$ catalysts are mainly composed of La, Cu, Ag and O elements (Fig. S4a), except for the reference element carbon, no signal of other impurity elements was detected, and the interference of other elements on the subsequent evaluation of CO_2RR properties is basically eliminated. The O 1 s XPS spectra of the $L_{2-x}A_xCO$ catalysts is shown in Fig. 2a. The four peaks at about 533.3, 530.8, 529.9, and 528.6 eV are indexed to the physical adsorption oxygen species on the surface (denoted as O_{surf}), the chemisorbed oxygen on the perovskite surface (denoted as O_{ads}), highly oxidative oxygen species (O_2^{2-}/O^-, corresponding to oxygen vacancies), and the surface lattice oxygen (denoted as O_{latt}), respectively [20,32,33]. Based on the relative peak areas, the concentrations of surface oxygen vacancies in $L_{2-x}A_xCO$ catalysts were computed as follows: 0 (L_2CO), 15.12% ($L_{1.9}A_{0.1}CO$), 15.23% ($L_{1.8}A_{0.2}CO$), 17.92% ($L_{1.7}A_{0.3}CO$), 22.02% ($L_{1.6}A_{0.4}CO$), and 24.28% ($L_{1.5}A_{0.5}CO$), respectively. Iodimetry experiments were conducted to quantify the amount of oxygen vacancies in the synthesized perovskite oxides. The results, as depicted in Fig. S5, reveal the following percentages of oxygen vacancies in the respective samples: 2.1% (L_2CO), 13.21% ($L_{1.9}A_{0.1}CO$), 14.22% ($L_{1.8}A_{0.2}CO$), 16.83% ($L_{1.7}A_{0.3}CO$), 21.34% ($L_{1.6}A_{0.4}CO$), and 23.35% ($L_{1.5}A_{0.5}CO$), respectively. These findings are in good agreement with the XPS results. It is worth noting that there exists a discrepancy in the measured oxygen vacancy concentrations between these two methods, primarily due to the significant different properties in the surface and bulk of the samples. EPR spectroscopy was utilized to further study the quantity of oxygen vacancies in $L_{2-x}A_xCO$ catalysts by detecting the presence of unpaired electrons in them. As shown in Fig. 2c, all $L_{2-x}A_xCO$ catalysts display obvious EPR signals at g = 2.003. The order of EPR signals intensity is as follows: L_2CO < $L_{1.9}A_{0.1}CO$ < $L_{1.8}A_{0.2}CO$ < $L_{1.7}A_{0.3}CO$ < $L_{1.6}A_{0.4}CO$ < $L_{1.5}A_{0.5}CO$, indicating that the introduction of Ag doping will generate a higher concentration of oxygen vacancies in these catalysts, and the surface oxygen vacancies increased with Ag doping. Fig. S4d displays the Ag 3d region of the XPS spectra of $L_{2-x}A_xCO$ samples. The prominent peaks positioned at binding energies of 368 and 374 eV correspond to the Ag 3d5/2 and Ag 3d3/2 states, respectively, featuring a spin-orbit splitting of 6.0 eV. The La 3d (Fig. S4b), Cu 2p (Fig. S4c), and Cu LMM (Fig. 2b) XPS spectra in the $L_{2-x}A_xCO$ catalysts are also analyzed to further confirm the change of oxygen vacancies in the samples. After doping Ag into $L_{2-x}A_xCO$ catalysts, the valence state of La^{3+} in these samples does not change, while the introduction of Ag^+ at A-site ions implies that the valence state of partial Cu changes from Cu^{2+} to Cu^+. Among them, the average valence states of Cu in $L_{1.9}A_{0.1}CO$, $L_{1.8}A_{0.2}CO$, $L_{1.7}A_{0.3}CO$, $L_{1.6}A_{0.4}CO$ and $L_{1.5}A_{0.5}CO$ are slightly changed, and the values range is from $+1.67$ to $+1.71$. These values are lower than the $(+2)$ valence state observed in L_2CO (Table S3). Perovskite oxides, in comparison to other metal oxides, possess a unique advantage in terms of their crystal structure flexibility. This flexibility allows for the accommodation of metal cations in unconventional or mixed valence states, consequently leading to an increased presence of oxygen vacancies within the material's structure [44,45]. Therefore, according to the electroneutrality principle, the $L_{2-x}A_xCO$ catalysts have more oxygen vacancies when more Ag substitution occurs at the A site. Notably, in the $L_{2-x}A_xCO$ catalysts, Cu^+ also increases gradually due to the ionic substitution at the A site, which changes the angle and length of the Cu-O bond. At the same time, it can be seen that the coordination relationship between Cu^+ and the corresponding O^{2-} ion is quite different from that of Cu^+ and O^{2-} ions in the traditional Cu_2O catalysts. This difference in coordination may give rise to intriguing catalytic properties.

Our findings suggest that oxygen vacancies may play a crucial role in the performance of CO_2RR. To verify this mechanism, we established two distinct density functional theory (DFT) models based on the XRD
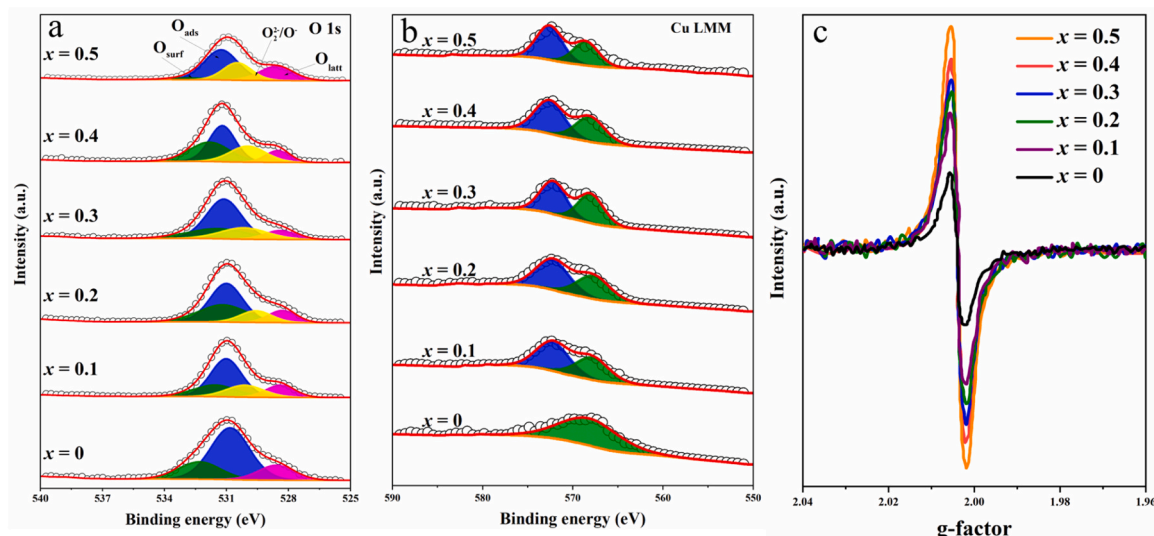
Fig. 2. (a) O 1s and (b) Cu LMM XPS spectra of the $L_{2-x}A_xCO$ samples. (c) EPR spectra of the $L_{2-x}A_xCO$ samples.

standard cards to explore the effect of Ag doping on the formation of oxygen vacancy formation. The first model is created by removing surface oxygen atoms of La_2CuO_4 (111) to generate an oxygen vacancy on the surface, denoted as O_V-LCO, as shown in Fig. 3a. The second model is a LaAgCuO (111) surface model with an oxygen vacancy, denoted as O_V-LACO, the surface is created by substituting the La atom in LCO (111) with an Ag atom to form LACO (111), and then removing one surface oxygen atom on the surface, as shown in Fig. 3b. We observe that the oxygen vacancy formation energy on O_V-LACO is the lowest at 3.89 eV, which is lower than that of LCO at 4.22 eV. This indicates that Ag doping can lower the formation energy and make it easier to form oxygen vacancies. Additionally, our calculations show that the bond angle (Cu−O−Cu) between O_{latt} and adjacent Cu atom increases to 167.95°, which is higher than that of LCO (148.24°). The significantly short Ag−O bond than La−O bond may be a contributor to the creation of oxygen vacancies after Ag doping. In summary, the surface oxygen vacancies of $L_{2-x}A_xCO$ catalysts can be rationally controlled by Ag doping engineering, which may lead to interesting catalytic performance.

Furthermore, DFT calculations were performed to forecast the CO_2RR performance of the catalysts, aiming to comprehend their distinctive electrocatalytic behaviors. In conjunction with XRD and XPS data analysis, it was observed that with Ag doping exceeding 0.2, a secondary phase emerges. Subsequently, DFT calculations were executed on the O_V-L_2CO (111) and O_V-$L_{1.8}A_{0.2}CO$ (111) surfaces to validate the real structure and composition of the $L_{2-x}A_xCO$ catalysts [32,46]. Fig. 4a shows the D-orbital projected density of states (PDOS) for Cu 3d band of O_V-L_2CO (111) and O_V-$L_{1.8}A_{0.2}CO$ (111) catalysts, respectively. According to the D-band theory, the occupied states of metal atoms on the catalyst surface and the distribution of D-orbital electrons are closely related to surface chemisorption. When molecular chemisorption occurs on a metal surface, the position of the D-band center relative to the Fermi energy level can predict the catalytic activity of the catalyst. The proximity to the Fermi level corresponds to heightened adsorption strength between the metal and the adsorbed species. The calculated value of Cu 3d band center is −2.32 eV for O_V-$L_{1.8}A_{0.2}CO$ (111), which is closer to the Fermi level than −2.40 eV of O_V-L_2CO (111). This result further confirms that Ag doping can gradually shift the D-band center towards the Fermi level, thereby increasing the adsorption strength of the intermediate species. This means that the moderate introduction of Ag can modulate the electronic structure of the L_2CO catalyst, bringing the D-band center closer to the Fermi level, thus facilitating electron transfer. To explore the distribution of the primary electrolytic products, we examined the associated reaction pathways,

encompassing $H^+ \rightarrow {}^*H \rightarrow H_2$ and ${}^*CO \rightarrow {}^*CHO \rightarrow {}^*OCHCHO^* \rightarrow C_2H_4$ (Figs. S6, S7) [47]. The relative free energies of basic steps in HER and CO_2RR to C_2H_4 were calculated. Since HER vied with CO_2RR during electrolysis process, we initially assessed the Gibbs free energy profiles for HER (Fig. 4b) to elucidate whether Ag doping would inhibit HER. Generally, the free energy of hydrogen adsorption is considered to be a reliable descriptor for evaluating the activity of HER [48]. Specifically, higher absolute values of the free energy indicate a greater difficulty in H adsorption and/or protonation, and thus lower HER activity. Compared with the O_V-L_2CO surface with a free energy of 0.72 eV, the O_V-$L_{1.8}A_{0.2}CO$ surface showed a significantly higher absolute value (0.86 eV), confirming that Ag doping can effectively suppress HER and thus facilitate CO_2RR. It has been previously established that the formation of C_2 products during CO_2RR depends primarily on the dimerization of ${}^*CHO$ species [42]. Based on this, the energy distribution of the key reaction intermediates for the production of C_2H_4 on the surfaces of the two catalysts was calculated (Fig. 4c, d). For the O_V-$L_{1.8}A_{0.2}CO$ (111) surface, Ag doping is more likely to form oxygen vacancies, and the energy barrier of rate-determining step (RDS, ${}^*CHO + {}^*CHO \rightarrow {}^*OCHCHO^*$) of C_2H_4 formation is 0.21 eV, which is much lower than that (0.68 eV) for O_V-L_2CO (Fig. 4e). As shown in Fig. 3, relative to O_V-LCO (111), Ag doping leads to the generation of oxygen vacancies, thus altering the catalyst's geometric structure. On the O_V-LACO (111) surface, the distance between Cu−O atoms increases to 2.03 Å, while on the O_V-LCO (111) surface, the Cu−O distance is only 1.91 Å. This results in a change in the distance between two adjacent Cu atoms, as depicted in Fig. S8. These changes exhibit varying degrees of geometric compatibility with the ${}^*OCHCHO^*$ intermediate. On the O_V-LCO (111) surface, the distance between adjacent Cu atoms is 3.55 Å, whereas on the O_V-LACO (111) surface, it is 3.91 Å, which is closer to the length of the intermediate, resulting in a higher degree of matching. Where the distance between two adjacent Cu atoms on the O_V-LCO (111) surface is 3.55 Å, and on the O_V-LACO (111) surface, it is 3.91 Å, closer to the length of the ${}^*OCHCHO^*$ intermediate (3.96 Å). This improved geometric matching significantly reduces the energy barrier for the formation of the ${}^*OCHCHO^*$ intermediate, ultimately decreasing the relative energy required for C_2H_4 formation from 2.44 eV on the O_V-L_2CO (111) surface to 0.78 eV on the O_V-$L_{1.8}A_{0.2}CO$ (111) surface. Consequently, Ag doping aids in better matching the geometric structure of the ${}^*OCHCHO^*$ intermediate with Cu active sites, enhancing the C−C coupling ability on the O_V-$L_{1.8}A_{0.2}CO$ (111) surface and effectively promoting the dimerization reaction of ${}^*CHO - {}^*CHO$, potentially facilitating the conversion of CO_2 to C_2 products.
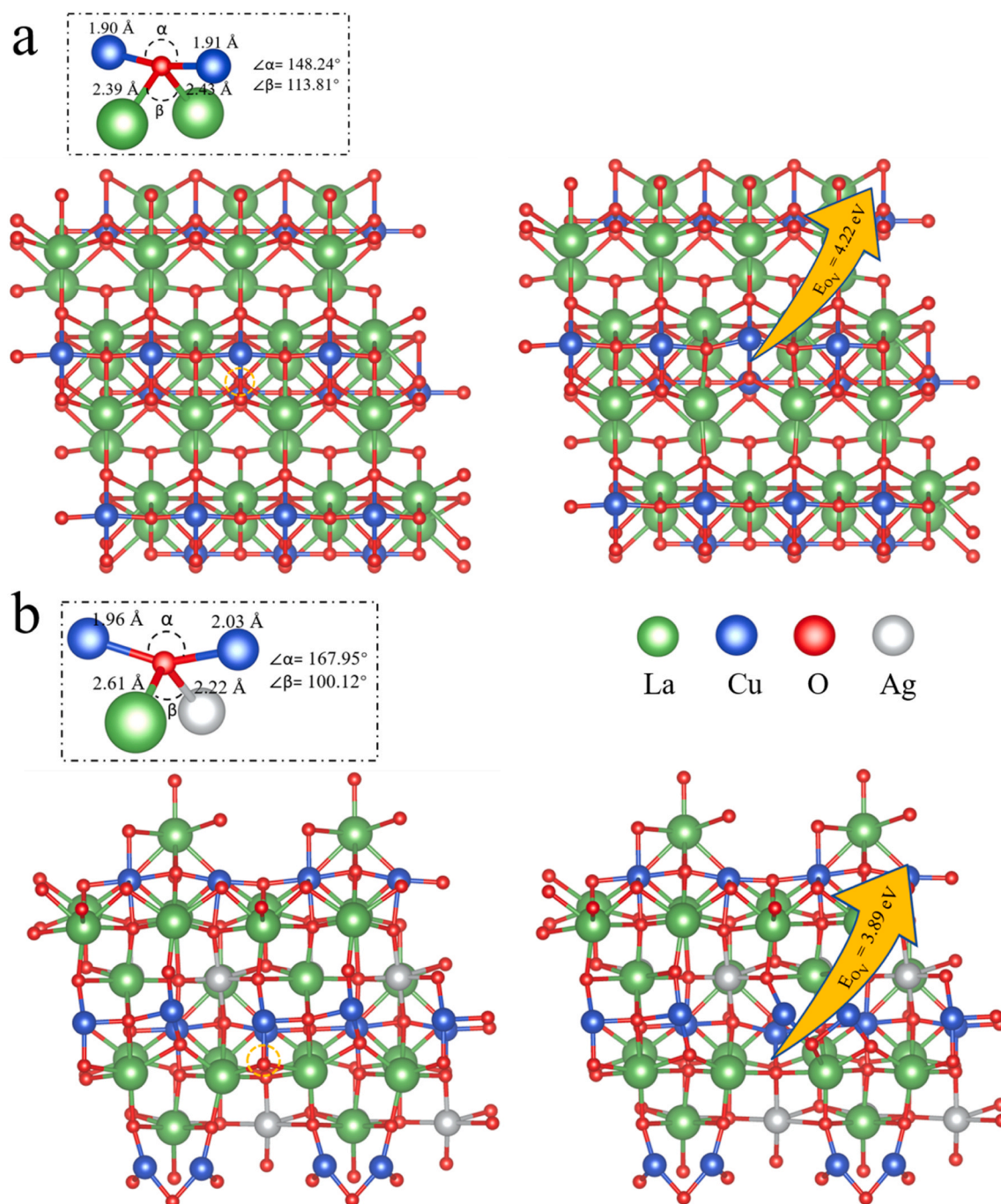
Fig. 3. (a) (111) surfaces of LCO and O_V-LCO. (b) (111) surfaces of LACO and O_V-LACO.

Linear sweep voltammetry (LSV) curves of $L_{2-x}A_xCO$ catalysts in Ar- and CO_2-saturated 0.5 M $KHCO_3$ aqueous solution were measured to preliminarily verified their CO_2RR catalytic activity (Fig. S9). The LSV curve showed that the current density in CO_2-saturated $KHCO_3$ solution was much higher than that in Ar-saturated environment in the whole applied potential region. Subsequently, gas chromatograph (GC) and nuclear magnetic resonance (NMR) methods can be used to analyze the Faradaic efficiency (FE) of the catalyst for gas and liquid products during the electrolysis process, thereby better evaluating the CO_2RR performance of the catalysts under different applied potentials (from −0.8 to −1.3 V) in the CO_2-saturated electrolyte. Figs. 5a-f and S10 exhibit the FE and current density (j) of the $L_{2-x}A_xCO$ catalysts for CO_2RR at different applied potentials, respectively. The products after electrolysis of these catalysts were various, among which the gaseous products are

H_2, CO, CH_4, and C_2H_4, and the liquid products including HCOOH and C_2H_5OH (Fig. S11). The CO_2RR activity and selectivity of $L_{2-x}A_xCO$ catalysts under different potentials were systematically investigated. Remarkably, within the range of applied potentials, a smaller value of FE_{H_2} indicated that the catalysts effectively inhibited competitive HER, and the catalyst had better CO_2RR activity (Fig. 5a-f). The FEs of various CO_2RR products obtained after electrolysis of the $L_{2-x}A_xCO$ catalysts showed similar trends. Therefore, we selected the most representative $L_{1.8}A_{0.2}CO$ as a proof-of-concept example to further systematically analyze the activity and selectivity under applied potentials (from −0.8 to −1.3 V). At a low cathodic applied potential of − 0.8 V, the main products were CO and HCOOH due to the two-electron transfer-dominated reduction. As the applied potential gradually shifted to a more negative direction, the two-electron transfer reduction was gradually
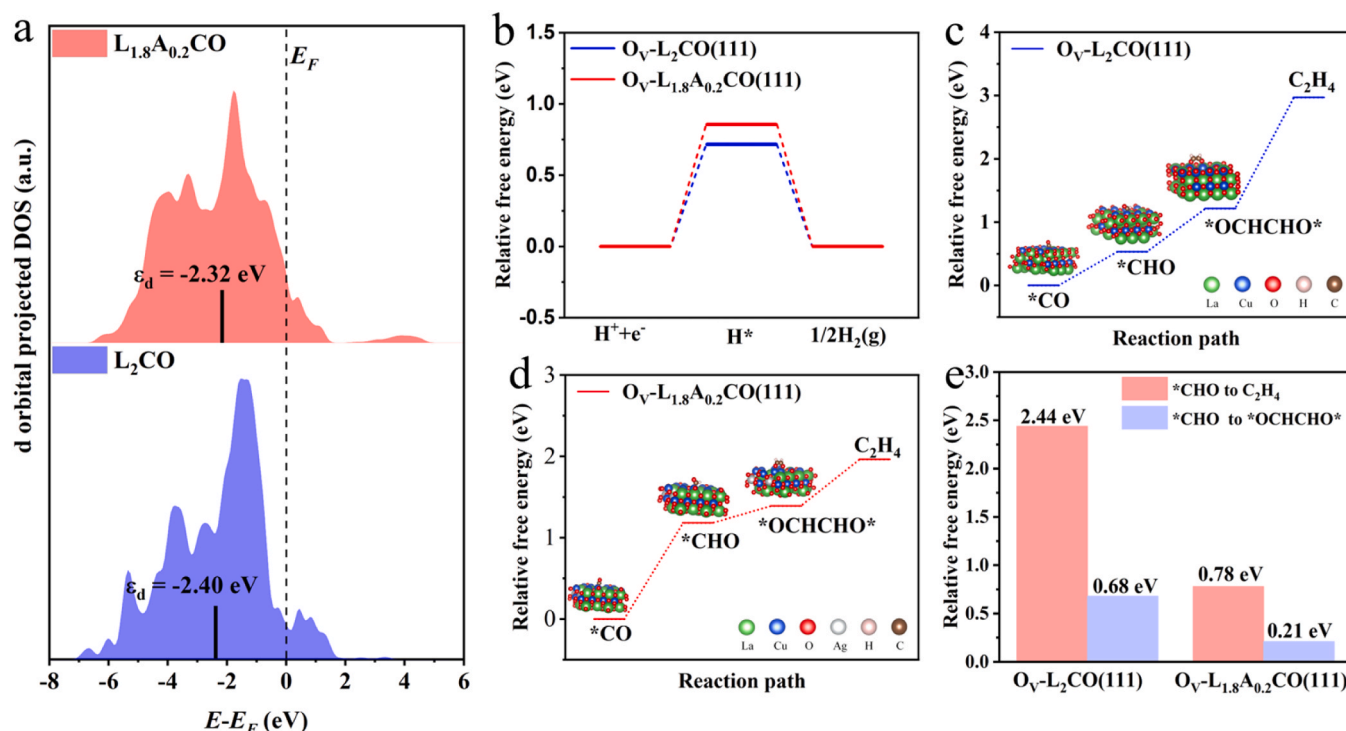
Fig. 4. (a) The projected density of states (PDOS) of Cu 3d orbitals for O_V-L_2CO (111) and O_V-$L_{1.8}A_{0.2}$CO (111). (b-d) The calculated free energy diagrams of CO_2RR to HER and C_2H_4 on O_V-L_2CO and O_V-$L_{1.8}A_{0.2}$CO surfaces, respectively. (e) Comparison of reaction energies for *CHO to C_2H_4 and *CHO to *OCHCHO* on the two surfaces.

replaced by the twelve-electron/proton transfer reduction, which made the catalytic products mainly C_2H_4 and C_2H_5OH. There is also a small amount of eight-electron transfer reduction, and the product is only CH_4. To be specific, when the applied potential ranged from -0.8 to -1.1 V, the Faradaic efficiency of single-carbon (C_1, e.g., CO, CH_4, and HCOOH) products decreased gradually, while that of multi-carbon (C_2, e.g., C_2H_4 and C_2H_5OH) products increased. Nevertheless, when the applied potential exceeded -1.1 V, FE_{H_2} will increase making the system difficult to suppress HER and resulting in a decrease of the FE_{CO_2RR}. By comparing the results of all electrolysis products, it can be found that almost all catalysts exhibit excellent performance at -1.1 V (Fig. S12); therefore, the CO_2RR performance of the six $L_{2-x}A_xCO$ catalysts at -1.1 V were compared and analyzed.

The test results are in line with expectations, Ag doping caused the A-site cation substitution and the formation of oxygen vacancies in the $L_{2-x}A_xCO$ catalysts, which had a significant impact on the performance of CO_2RR (Fig. 5g, h). Specifically, $L_{1.8}A_{0.2}CO$ catalyst has much higher FE_{CO_2RR} and j_{CO_2RR}, together with much lower FE_{H_2} and j_{H_2} than other catalysts. In other words, at the applied potential of -1.1 V, the Ag doping amount x proved a volcano dependence on the CO_2RR of the $L_{2-x}A_xCO$ catalysts, with a maximum value corresponding to 0.2, that is, the $L_{1.8}A_{0.2}CO$ catalyst has the strongest CO_2RR activity (Fig. 5g). When the amount of Ag doping is low, cationic replacement occurs in the A site of the catalysts, generating oxygen vacancies, which can better suppress HER. However, at higher Ag doping amount, the catalysts would produce a large amount of CuO, which limited the performance of CO_2RR. Similar to the evolution in $FE_{CO_2RR}(j_{CO_2RR})$ and $FE_{H_2}(j_{H_2})$, the $FE_{C_1}(j_{C_1})$ and $FE_{C_2}(j_{C_2})$ also adhered to the patterns of volcano-type and inverted volcano-type behavior, respectively. Notably, both trends converged at the same peak point at $x = 0.2$. (Fig. 5h). As expected, among the six catalysts, the $L_{1.8}A_{0.2}CO$ catalyst exhibited the maximum FE_{C_2} and j_{C_2} values of 86.4% and 22.7 mA cm^{-2}, respectively. These values were notably superior to those achieved by the L_2CO (67% and 16.6 mA cm^{-2}), $L_{1.9}A_{0.1}CO$ (78% and 20 mA cm^{-2}), $L_{1.7}A_{0.3}CO$ (80% and 19 mA cm^{-2}), $L_{1.6}A_{0.4}CO$ (66% and 17 mA cm^{-2}) and $L_{1.5}A_{0.5}CO$

(62% and 16 mA cm^{-2}). Whereas for C_1, the FE_{C_1} and j_{C_1} values exhibited a descending sequence: $L_{1.5}A_{0.5}CO$ (40% and 11.8 mA cm^{-2}) $> L_{1.6}A_{0.4}CO$ (28.6% and 7.4 mA cm^{-2}) $> L_{1.7}A_{0.3}CO$ (27% and 6.4 mA cm^{-2}) $> L_2CO$ (21% and 5.2 mA cm^{-2}) $> L_{1.9}A_{0.1}CO$ (14% and 3.6 mA cm^{-2}) $> L_{1.8}A_{0.2}CO$ (11% and 3 mA cm^{-2}). This implies that higher Ag doping results in increased CuO content, which effectively enhances the conversion of CO_2 to C_1.

When comparing the single selectivity of the electrolytic products, it can be found that the single selectivity of C_2H_4 on $L_{1.8}A_{0.2}CO$ is also the best among all catalysts (Fig. 5i). Based on the aforementioned findings, it can be deduced that the generation of oxygen vacancies in the A-site ion replacement process of the $L_{2-x}A_xCO$ catalysts can better promote the development of CO_2RR to the formation of C_2. Furthermore, the optimal quantity of Ag doping manifests at $x = 0.2$. Significantly, when juxtaposed with the majority of documented Cu-based perovskite oxidation catalysts, the $L_{1.8}A_{0.2}CO$ catalyst demonstrates exceptional activity and superior selectivity towards C_2 products (Table S4) [20,32,46]. Furthermore, we explored the CO_2RR stability of the $L_{1.8}A_{0.2}CO$ catalyst utilizing a standard H-type cell, as it effectively demonstrates the intrinsic stability of catalysts. Fig. 5j reveals that the $L_{1.8}A_{0.2}CO$ catalyst also exhibits considerable electrochemical CO_2 reduction stability during 15 h potentiostatic electrolysis -1.1 V. The total current density and $FE_{C_2H_4}$ product was about 25 mA cm^{-2} and 70%, respectively, without a significant decline during 15 h stability test. In brief, the as-prepared $L_{1.8}A_{0.2}CO$ catalyst is competitive in terms of CO_2RR performance for C_2H_4 products compared with previously reported Cu-based oxides catalysts. In order to investigate whether Ag can form bimetallic tandem catalysis with L_2CO catalyst to improve FE_{C_2} products during CO_2RR process, we prepared L_2CO/Ag catalysts for related electrochemical tests (Fig. S14). The results showed that the main reduction product was CO, and the production of C_2 products was rare, which could rule out the influence of tandem catalysis.

A series of characterizations were carried out on the electrolyzed $L_{1.8}A_{0.2}CO$ catalyst to explore whether the structure of the catalyst changed during the CO_2 cathodic electrolysis. After 1 h of electrolysis,
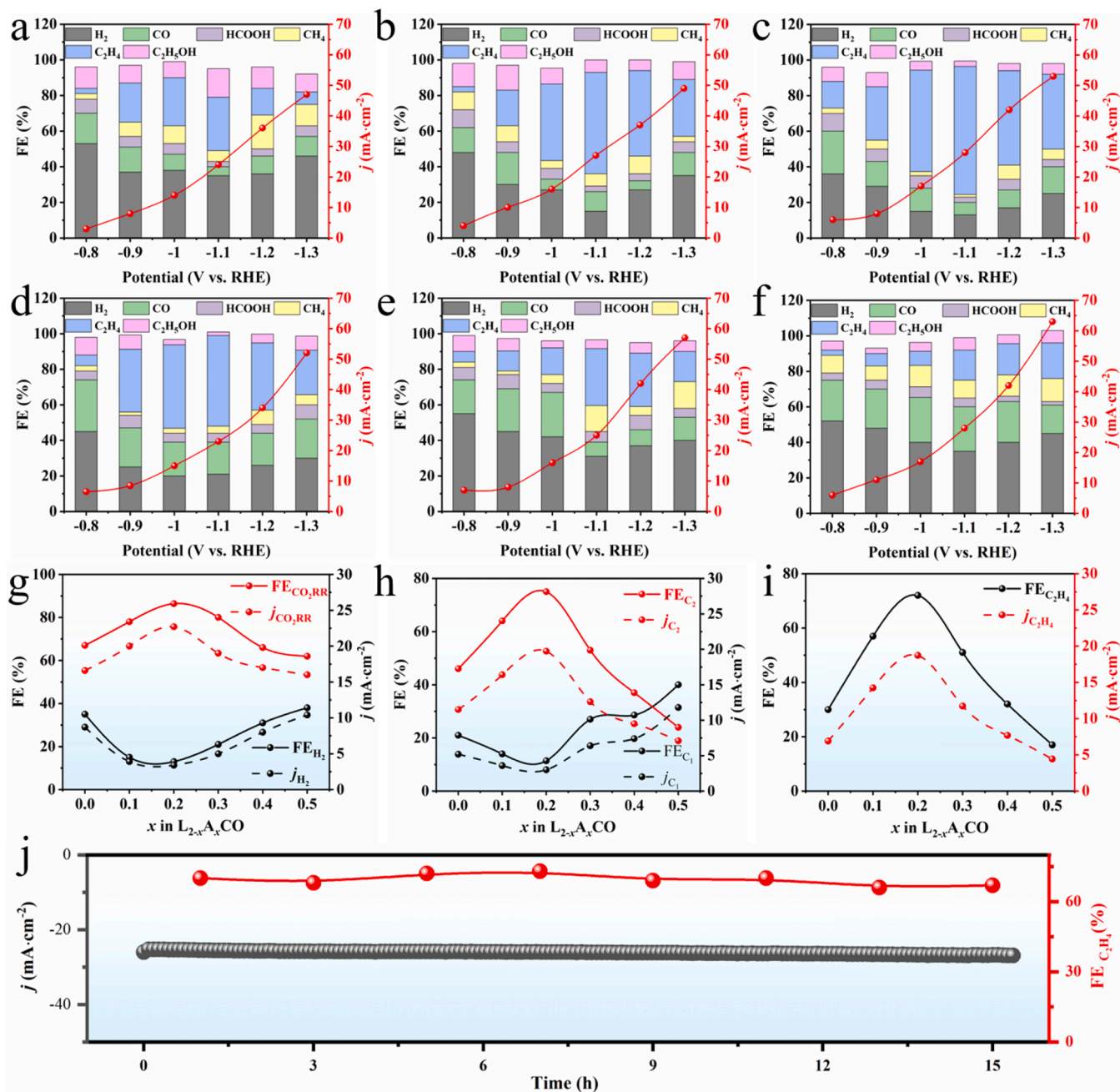
Fig. 5. (a-f) FEs of various CO_2RR products over the $L_{2-x}A_xCO$ catalysts: (a) L_2CO, (b) $L_{1.9}A_{0.1}CO$, (c) $L_{1.8}A_{0.2}CO$, (d) $L_{1.7}A_{0.3}CO$, (e) $L_{1.6}A_{0.4}CO$ and (f) $L_{1.5}A_{0.5}CO$. (g) The current densities and FEs of H_2 and CO_2RR over the $L_{2-x}A_xCO$ catalysts at -1.1 V as a function of the x values. (h) Dependence of the current densities and FEs of C_1 and C_2 over the $L_{2-x}A_xCO$ catalysts at -1.1 V on the x values. (i) The current densities and FEs of C_2H_4 over the $L_{2-x}A_xCO$ catalysts at -1.1 V as a function of the x values. (j) Chronoamperometry tests of the $L_{1.8}A_{0.2}CO$ catalyst at -1.1 V for 15 h CO_2 electroreduction.

the XRD pattern of the cathode perovskite indicates the retention of the La_2CuO_4 phase (Fig. 6a). SEM results show that although the surface of the $L_{1.8}A_{0.2}CO$ catalyst become rougher after the electrolysis, the overall particle morphology remain intact (Fig. 6b). Fig. 6c presents a typical HRTEM image of the $L_{1.8}A_{0.2}CO$ after the 1 h electrolytic stability test. The interplanar spaces of 0.37 nm corresponds to La_2CuO_4 (111). In addition to no changes in morphology, the distribution of elements did not change after the electrochemical process (Fig. 6d). EDS elemental mapping demonstrated a uniform distribution of La, Cu, O and Ag elements. These characterizations again confirmed that the $L_{1.8}A_{0.2}CO$ catalyst did not undergo obvious degradation during the electrolytic stability test. We selected the optimized $La_{1.8}Ag_{0.2}CuO_{4-\delta}$ catalyst to assess the oxygen vacancy status after 15 h of electrolysis, as shown in

Fig. S15a. The $La_{1.8}Ag_{0.2}CuO_{4-\delta}$ catalyst, even after 15 h of CO_2RR electrolysis, still exhibits a distinct EPR signal at g = 2.003, indicating the continued presence of oxygen vacancies. To verify whether the structure of the $La_{1.8}Ag_{0.2}CuO_{4-\delta}$ catalyst remains stable after long-term CO_2RR testing, we compared the XRD results at 1 h, 15 h, and 20 h, as shown in Fig. S15b. After 1 h of CO_2RR electrolysis, no significant peaks or impurities are observed in the XRD diffraction pattern, suggesting that the structure of $La_{1.8}Ag_{0.2}CuO_{4-\delta}$ remains unchanged. However, after 15 h, an enhancement of the Ag peak at around $2\theta = 43°$ is noticeable, indicating some silver segregation, but the overall structure of the catalyst remains unaltered. Continuing the electrolysis to 20 h results in the appearance of distinct impurity peaks in the XRD pattern, indicating a change in the catalyst's crystal structure, and a shift in the
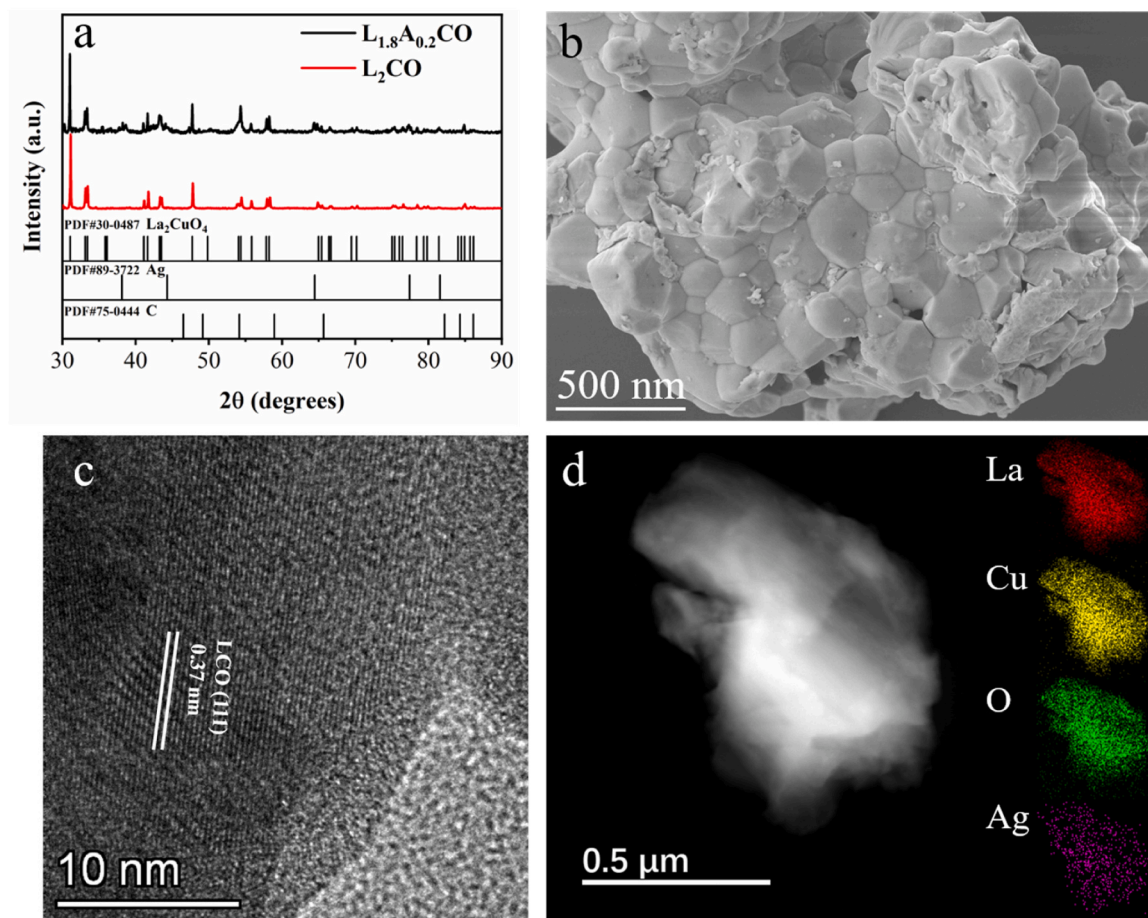
Fig. 6. (a) XRD patterns, (b) SEM image, (c) HRTEM image, and (d) EDS elemental mapping of the cathodized $L_{1.8}A_{0.2}CO$ perovskite oxide.

pH of the electrolyte has occurred. Longer electrolysis times lead to an unstable catalyst structure. Therefore, our stability testing for 15 h ensures that the catalyst structure remains unchanged.

To gain a deeper comprehension of the augmented CO_2RR activity and selectivity in $L_{2-x}A_xCO$ catalysts, we assessed the double layer capacitance (C_{dl}) values of these catalysts (Figs. 7a and S13). The C_{dl} values followed the subsequent order: $L_{1.5}A_{0.5}CO < L_{1.6}A_{0.4}CO < L_2CO < L_{1.7}A_{0.3}CO < L_{1.9}A_{0.1}CO < L_{1.8}A_{0.2}CO$, suggesting that an Ag doping amount of 0.2 can significantly enlarge the electrochemically active surface area (ECSA), this almost corresponds to the trend of CO_2RR performances. As depicted in Fig. 7b, the Nyquist plots and corresponding fitting outcomes for the $L_{2-x}A_xCO$ catalysts exhibit a comparable semicircular pattern. The inset illustrates the equivalent circuit model aligned with the charge-transfer control mechanism. The Electrochemical Impedance Spectroscopy (EIS) data of the concomitant charge-transfer controlled region can be effectively obtained through the equivalent circuit model. In general, the diameter of the semicircle in the Nyquist plots represents the typical interfacial charge transfer resistance (R_{ct}) at the electrode/electrolyte interface, which is the main obstacle to overcome, while the diffusion resistance is negligible [49, 50]. The results indicate that the R_{ct} of $L_{1.8}A_{0.2}CO$ is significantly lower than that of other catalysts, indicating that the significant transfer resistance of these catalysts is affected by the Ag doping, which has a great influence on the kinetics of CO_2RR. Due to the high electrical conductivity of Ag, the charge transfer resistance of the catalyst decreases significantly once doped with an appropriate amount of Ag (e.g., $x = 0.2$). To explore the interfacial reaction kinetics for C_2 formation, we examined the Tafel plots of CO_2RR on the catalysts (Fig. 7c). The Tafel slopes of $L_{1.9}A_{0.1}CO$ (214.3 mV dec^{-1}), $L_{1.8}A_{0.2}CO$ (168.4 mV dec^{-1}), $L_{1.7}A_{0.3}CO$ (178.4 mV dec^{-1}), $L_{1.6}A_{0.4}CO$ (193.6 mV dec^{-1}) and $L_{1.5}A_{0.5}CO$ (136.5 mV dec^{-1}) are all lower than that of pure L_2CO (246.5 mV dec^{-1}), indicating that Ag doping accelerated the electrode reaction rate and effectively promoted the kinetic process of electrocatalytic CO_2 to C_2. The relationship between Tafel slope and Ag doping amount in catalyst is shown in Fig. 7d. The Tafel slope for $L_{1.8}A_{0.2}CO$ (168.4 mV dec^{-1}) is significantly smaller than that for other catalysts, and lower Tafel slope means faster kinetic process, and the trend of Tafel slopes agrees well with the current activity related volcano plots as shown in Fig. 5h. Accordingly, these results further confirm that charge transport on the catalyst is an important factor affecting the change of CO_2RR performance, and the $L_{1.8}A_{0.2}CO$ catalyst has faster charge transfer and better CO_2RR activity. In addition, the adsorption properties, including the binding strength of reactive species on the catalytic sites, exert a pivotal influence on the CO_2RR performance. All catalysts were subjected to CO_2 temperature-programmed desorption (CO_2-TPD) tests, and the CO_2RR activity of these catalysts was combined to analyze the CO_2 adsorption capacity (Fig. 7e). As expected, the onset desorption temperature of CO_2 chemisorption by $L_{2-x}A_xCO$ catalysts increases in the following order: $L_{1.5}A_{0.5}CO$ (428 °C) $< L_2CO$ (431 °C) $< L_{1.6}A_{0.4}CO$ (432 °C) $< L_{1.7}A_{0.3}CO$ (442 °C) $< L_{1.9}A_{0.1}CO$ (450 °C) $< L_{1.8}A_{0.2}CO$ (462 °C). These results suggest that the chemisorption of CO_2 can be significantly enhanced by replacing the A-site ions with appropriate Ag doping. The most plausible explanation is that in the absence of CuO formation, a certain amount of oxygen vacancies will be formed in the catalyst after the A-site ion replacement without CuO generation, thus bringing more active sites for the chemisorption and activation of CO_2 molecules. Previous investigations have established that the chemisorption of CO_2 onto the catalyst surface is a pivotal prerequisite for initiating CO_2RR [46]. Moreover, the strength of adsorption exhibits a linear correlation with the CO_2RR activity. As shown in Fig. 7f,
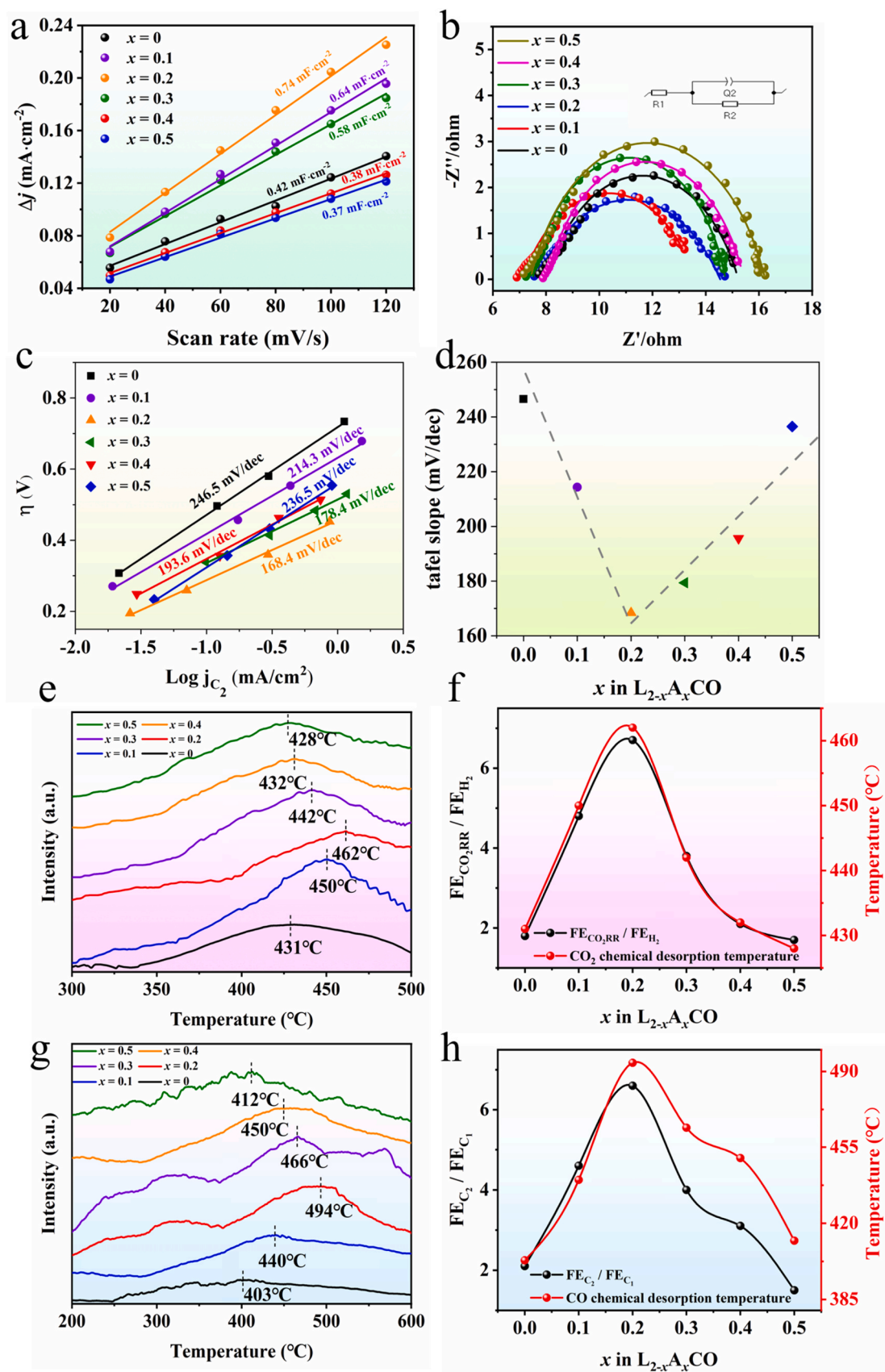
Fig. 7. (a) Linear fitting curves of the capacitive currents versus scan rates for the $L_{2-x}A_xCO$ catalysts. (b) Nyquist plots for the $L_{2-x}A_xCO$ catalysts. (c) Tafel slops for the $L_{2-x}A_xCO$ catalysts. (d) The Tafel slope as a function of the compositional fraction of Ag shows an inverted volcano type. (e) CO_2-TPD of the $L_{2-x}A_xCO$ catalysts. (f) Correlation of the FE_{CO_2RR}/FE_{H_2} over the $L_{2-x}A_xCO$ catalysts with the CO_2 chemical desorption temperature. (g) CO-TPD of the $L_{2-x}A_xCO$ catalysts. (h) Correlation of the FE_{C_2}/FE_{C_1} over the $L_{2-x}A_xCO$ catalysts with the CO chemical desorption temperature.

theFE$_{CO_2RR}$/FE$_{H_2}$ values for these catalysts were calculated as 1.8 (L$_2$CO), 4.8 (L$_{1.9}$A$_{0.1}$CO), 6.7 (L$_{1.8}$A$_{0.2}$CO), 3.8 (L$_{1.7}$A$_{0.3}$CO), 2.1 (L$_{1.6}$A$_{0.4}$CO) and 1.7 (L$_{1.5}$A$_{0.5}$CO), respectively. The FE ratios of CO$_2$RR/H$_2$ values followed a similar trend to the CO$_2$ adsorption capacity (Fig. 7e), which further supports the correlation between CO$_2$ chemisorption and the CO$_2$RR performance of L$_{2-x}$A$_x$CO catalysts. Therefore, the introduction of Ag$^+$ ions into the L$_{2-x}$A$_x$CO catalysts for A-site cation replacement and the regulation of oxygen vacancy in the catalysts can not only accelerate electron transfer, but also effectively adsorb and activate CO$_2$, thereby improving the catalytic activity of CO$_2$RR. Furthermore, the adsorption capacity of CO on these catalysts were examined by using the CO-TPD tests (Fig. 7g). In the CO$_2$RR process, the enhanced chemical adsorption capacity of CO plays a key role in promoting C−C coupling. Consequently, CO-TPD serves as a pragmatic approach to gauge the viability of *CO dimerization [46].

Similar to the CO$_2$-TPD, the CO chemisorption capacity of L$_{1.8}$A$_{0.2}$CO catalyst was still the highest, and the specific adsorption capacity increases successively: L$_2$CO (403 ℃) < L$_{1.5}$A$_{0.5}$CO (412 ℃) < L$_{1.9}$A$_{0.1}$CO (440 ℃) < L$_{1.6}$A$_{0.}$ $_4$CO (450 ℃) < L$_{1.7}$A$_{0.3}$CO (466 ℃) < L$_{1.8}$A$_{0.2}$CO (494 ℃) (Fig. 7g). Thus, it can be speculated that L$_{1.8}$A$_{0.2}$CO catalyst has the highest FE$_{C_2}$. As depicted in Fig. 7h, the FE$_{C_2}$/FE$_{C_1}$ values of these L$_{2-x}$A$_x$CO catalysts exhibited the same trend as their CO chemisorption capacities, which further indicated that CO chemisorption promoted the CO$_2$ −C$_2$ conversion process. Taken together, the doping of A-site Ag$^+$ ions in L$_{2-x}$A$_x$CO catalysts can not only improve the multi-electron/proton transfer ability, but also regulate the adsorption/activation of active species (such as CO$_2$ and CO) after catalysis, suppress HER, and promote C−C dimerization, thus optimizing both CO$_2$RR activity and the singular selectivity of C$_2$ products.

4. Conclusions

In summary, we designed a Ruddlesden-Popper layered perovskite La$_{2-x}$Ag$_x$CuO$_{4-\delta}$ catalysts with Ag substitution at the A site. In this study, the effect of Ag doping on the CO$_2$RR performance of La$_{2-x}$Ag$_x$CuO$_{4-\delta}$ catalysts and the structure-activity relationship were systematically studied. It also shows that A-site ion substitution is an effective strategy for improving CO$_2$RR performance. This substitution-induced generation of oxygen vacancies provides abundant active sites for CO$_2$ electrocatalysis, shifting the reaction pathway from a double-electron transfer reduction to a multi-electron/proton transfer reduction, thereby promoting the formation of C$_2$ products. Among them, a high FE of 86.4% with a partial current density of 22.7 mA cm^{-2} at − 1.1 V vs. RHE for C$_2$ products were achieved over this L$_{1.8}$A$_{0.2}$CO catalyst, showing the greatest activity and excellent stability to CO$_2$RR. Both experimental characterization and DFT calculations concurred in suggesting that the formation of oxygen vacancies facilitates the adsorption and activation of reactants, thereby optimizing the dimerization and/or hydrogenation of *CO intermediates. This work paves the way for the rational design of high-performance perovskite oxide catalysts for CO$_2$RR.

CRediT authorship contribution statement

Gang Dong: Methodology, Data curation, Formal analysis, Visualization, Writing – original draft. **Guo Wang**: Synthesis, Data curation, Formal analysis. **Jiarun Cheng**: Data curation, Formal analysis. **Meng Li**: Data curation, Formal analysis. **Zhifu Liang**: Writing – review & editing, Formal analysis. **Weiqiang Tang**: Simulations, Formal analysis. **Dongsheng Geng**: Conceptualization, Funding acquisition, Methodology, Validation, Writing – review & editing.

Declaration of Competing Interest

The authors declare that they have no known competing financial interests or personal relationships that could have appeared to influence the work reported in this paper.

Data availability

Data will be made available on request.

Acknowledgments

Appendix A. Supporting information

Supplementary data associated with this article can be found in the online version at doi:10.1016/j.apcatb.2023.123444.

References

[1] C.W. Li, M.W. Kanan, CO$_2$ reduction at low overpotential on Cu electrodes resulting from the reduction of thick Cu$_2$O films, J. Am. Chem. Soc. 134 (2012) 7231–7234.

[2] C.W. Li, J. Ciston, M.W. Kanan, Electroreduction of carbon monoxide to liquid fuel on oxide-derived nanocrystalline copper, Nature 508 (2014) 504–507.

[3] T.T.H. Hoang, S. Ma, J.I. Gold, P.J.A. Kenis, A.A. Gewirth, Nanoporous copper films by additive-controlled electrodeposition: CO$_2$ reduction catalysis, ACS Catal. 7 (2017) 3313–3321.

[4] M. Aresta, A. Dibenedetto, A. Angelini, Catalysis for the valorization of exhaust carbon: from CO$_2$ to chemicals, materials, and fuels. technological use of CO$_2$, Chem. Rev. 114 (2014) 1709–1742.

[5] D. Wakerley, S. Lamaison, F. Ozanam, N. Menguy, D. Mercier, P. Marcus, M. Fontecave, V. Mougel, Bio-inspired hydrophobicity promotes CO$_2$ reduction on a Cu surface, Nat. Mater. 18 (2019) 1222–1227.

[6] Z.W. Seh, J. Kibsgaard, C.F. Dickens, I. Chorkendorff, J.K. Norskov, T.F. Jaramillo, Combining theory and experiment in electrocatalysis: insights into materials design, Science 355 (2017), eaad4998.

[7] X. Lu, Y. Wu, X. Yuan, H. Wang, An integrated CO$_2$ electrolyzer and formate fuel cell enabled by a reversibly restructuring Pb-Pd bimetallic catalyst, Angew. Chem. Int. Ed. Engl. 58 (2019) 4031–4035.

[8] Y.Y. Birdja, E. Pérez-Gallent, M.C. Figueiredo, A.J. Göttle, F. Calle-Vallejo, M.T. M. Koper, Advances and challenges in understanding the electrocatalytic conversion of carbon dioxide to fuels, Nat. Energy 4 (2019) 732–745.

[9] C.G. Morales-Guio, E.R. Cave, S.A. Nitopi, J.T. Feaster, L. Wang, K.P. Kuhl, A. Jackson, N.C. Johnson, D.N. Abram, T. Hatsukade, C. Hahn, T.F. Jaramillo, Improved CO$_2$ reduction activity towards C2+ alcohols on a tandem gold on copper electrocatalyst, Nat. Catal. 1 (2018) 764–771.

[10] X. Chen, J. Chen, N.M. Alghoraibi, D.A. Henckel, R. Zhang, U.O. Nwabara, K. E. Madsen, P.J.A. Kenis, S.C. Zimmerman, A.A. Gewirth, Electrochemical CO$_2$-to-ethylene conversion on polyamine-incorporated Cu electrodes, Nat. Catal. 4 (2021) 20–27.

[11] S. Nitopi, E. Bertheussen, S.B. Scott, X. Liu, A.K. Engstfeld, S. Horch, B. Seger, I.E. L. Stephens, K. Chan, C. Hahn, J.K. Norskov, T.F. Jaramillo, I. Chorkendorff, Progress and perspectives of electrochemical CO$_2$ reduction on copper in aqueous electrolyte, Chem. Rev. 119 (2019) 7610–7672.

[12] Z. Sun, Y. Hu, D. Zhou, M. Sun, S. Wang, W. Chen, Factors influencing the performance of copper-bearing catalysts in the CO$_2$ reduction system, ACS Energy Lett. 6 (2021) 3992–4022.

[13] S. Gao, Y. Lin, X. Jiao, Y. Sun, Q. Luo, W. Zhang, D. Li, J. Yang, Y. Xie, Partially oxidized atomic cobalt layers for carbon dioxide electroreduction to liquid fuel, Nature 529 (2016) 68–71.

[14] C. Choi, T. Cheng, M. Flores Espinosa, H. Fei, X. Duan, W.A. Goddard 3rd, Y. Huang, A highly active star decahedron Cu nanocatalyst for hydrocarbon production at low overpotentials, Adv. Mater. 31 (2019), e1805405.

[15] L. Zhang, Z.J. Zhao, J. Gong, Nanostructured materials for heterogeneous electrocatalytic CO$_2$ reduction and their related reaction mechanisms, Angew. Chem. Int. Ed. Engl. 56 (2017) 11326–11353.

[16] K.P. Kuhl, E.R. Cave, D.N. Abram, T.F. Jaramillo, New insights into the electrochemical reduction of carbon dioxide on metallic copper surfaces, Energy Environ. Sci. 5 (2012) 7050–7059.

[17] P. Grosse, A. Yoon, C. Rettenmaier, A. Herzog, S.W. Chee, B. Roldan Cuenya, Dynamic transformation of cubic copper catalysts during CO$_2$ electroreduction and its impact on catalytic selectivity, Nat. Commun. 12 (2021) 6736.

[18] Y.A. Wu, I. McNulty, C. Liu, K.C. Lau, Q. Liu, A.P. Paulikas, C.-J. Sun, Z. Cai, J. R. Guest, Y. Ren, V. Stamenkovic, L.A. Curtiss, Y. Liu, T. Rajh, Facet-dependent active sites of a single Cu$_2$O particle photocatalyst for CO$_2$ reduction to methanol, Nat. Energy 4 (2019) 957–968.

[19] Z. Geng, X. Kong, W. Chen, H. Su, Y. Liu, F. Cai, G. Wang, J. Zeng, Oxygen vacancies in ZnO nanosheets enhance CO_2 electrochemical reduction to CO, Angew. Chem. Int. Ed. Engl. 57 (2018) 6054–6059.

[20] J. Zhu, Y. Wang, A. Zhi, Z. Chen, L. Shi, Z. Zhang, Y. Zhang, Y. Zhu, X. Qiu, X. Tian, X. Bai, Y. Zhang, Y. Zhu, Cation-deficiency-dependent CO_2 electroreduction over copper-based Ruddlesden-Popper perovskite oxides, Angew. Chem. Int. Ed. Engl. 61 (2022), e202111670.

[21] H. Zheng, Y. Zhang, Y. Wang, Z. Wu, F. Lai, G. Chao, N. Zhang, L. Zhang, T. Liu, Perovskites with enriched oxygen vacancies as a family of electrocatalysts for efficient nitrate reduction to ammonia, Small 19 (2023), e2205625.

[22] S. Gao, Z. Sun, W. Liu, X. Jiao, X. Zu, Q. Hu, Y. Sun, T. Yao, W. Zhang, S. Wei, Y. Xie, Atomic layer confined vacancies for atomic-level insights into carbon dioxide electroreduction, Nat. Commun. 8 (2017) 14503.

[23] L. Zhang, L. Wang, H. Lin, Y. Liu, J. Ye, Y. Wen, A. Chen, L. Wang, F. Ni, Z. Zhou, S. Sun, Y. Li, B. Zhang, H. Peng, A lattice-oxygen-involved reaction pathway to boost urea oxidation, Angew. Chem. Int. Ed. Engl. 58 (2019) 16820–16825.

[24] Z. Shi, Z. Yu, R. Jiang, J. Huang, Y. Hou, J. Chen, Y. Zhang, H. Zhu, B. Wang, H. Pang, MOF-derived M-OOH with rich oxygen defects by in situ electro-oxidation reconstitution for a highly efficient oxygen evolution reaction, J. Mater. Chem. A 9 (2021) 11415–11426.

[25] L. Yan, Y. Lin, X. Yu, W. Xu, T. Salas, H. Smallidge, M. Zhou, H. Luo, $La_{0.8}Sr_{0.2}MnO_3$-based perovskite nanoparticles with the A-site deficiency as high performance bifunctional oxygen catalyst in alkaline solution, ACS Appl. Mater. Interfaces 9 (2017) 23820–23827.

[26] Y. Lv, W. Yao, X. Ma, C. Pan, R. Zong, Y. Zhu, The surface oxygen vacancy induced visible activity and enhanced UV activity of a ZnO_{1-x} photocatalyst, Catal. Sci. Technol. 3 (2013) 3136–3146.

[27] Y. Sun, S. Gao, F. Lei, C. Xiao, Y. Xie, Ultrathin two-dimensional inorganic materials: new opportunities for solid state nanochemistry, Acc. Chem. Res. 48 (2015) 3–12.

[28] Q. Ji, L. Bi, J. Zhang, H. Cao, X.S. Zhao, The role of oxygen vacancies of ABO_3 perovskite oxides in the oxygen reduction reaction, Energy Environ. Sci. 13 (2020) 1408–1428.

[29] X. Li, H. Zhao, J. Liang, Y. Luo, G. Chen, X. Shi, S. Lu, S. Gao, J. Hu, Q. Liu, X. Sun, A-site perovskite oxides: an emerging functional material for electrocatalysis and photocatalysis, J. Mater. Chem. A 9 (2021) 6650–6670.

[30] X. Xu, Y. Pan, Y. Zhong, R. Ran, Z. Shao, Ruddlesden–Popper perovskites in electrocatalysis, Mater. Horiz. 7 (2020) 2519–2565.

[31] S. Royer, D. Duprez, F. Can, X. Courtois, C. Batiot-Dupeyrat, S. Laassiri, H. Alamdari, Perovskites as substitutes of noble metals for heterogeneous catalysis: dream or reality, Chem. Rev. 114 (2014) 10292–10368.

[32] S. Chen, Y. Su, P. Deng, R. Qi, J. Zhu, J. Chen, Z. Wang, L. Zhou, X. Guo, B.Y. Xia, Highly selective carbon dioxide electroreduction on structure-evolved copper perovskite oxide toward methane production, ACS Catal. 10 (2020) 4640–4646.

[33] L. He, Y. Zhang, Y. Zang, C. Liu, W. Wang, R. Han, N. Ji, S. Zhang, Q. Liu, Promotion of A-site Ag-doped perovskites for the catalytic oxidation of soot: synergistic catalytic effect of dual active sites, ACS Catal. 11 (2021) 14224–14236.

[34] X. Shi, J. Guo, T. Shen, A. Fan, S. Yuan, J. Li, Enhancement of Ce doped La–Mn oxides for the selective catalytic reduction of NO_x with NH_3 and SO_2 and/or H_2O resistance, Chem. Eng. J. 421 (2021), 129995.

[35] G. Dong, T. Sun, F. Ji, Y. Liu, S. Zhang, H. Zhang, X. Liu, Polycrystalline $La_{0.845}Sr_{0.155}MnO_3$:Ag ceramics ($0 \leq x \leq 0.5$) with room-temperature TCR and MR

[36] for improved uncooling photoelectric and magnetic devices, Ceram. Int. 45 (2019) 12162–12168.

H.A. Tahini, X. Tan, U. Schwingenschlögl, S.C. Smith, Formation and migration of oxygen vacancies in $SrCoO_3$ and their effect on oxygen evolution reactions, ACS Catal. 6 (2016) 5565–5570.

[37] F. He, M. Hou, F. Zhu, D. Liu, H. Zhang, F. Yu, Y. Zhou, Y. Ding, M. Liu, Y. Chen, Building efficient and durable hetero-interfaces on a perovskite-based electrode for electrochemical CO_2 reduction, Adv. Energy Mater. 12 (2022), 2202175.

[38] G. Dong, T. Sun, Y. Liu, S. Zhang, X. Liu, Structural and electrical properties of $La_{0.67}(Ca_{0.3}Sr_{0.03})MnO_3$ composites prepared with added Ag, J. Alloy. Compd. 794 (2019) 365–373.

[39] G. He, X. Liu, R. Li, D. Zhai, Y. Liu, C. Xie, P. Hu, Q. Zhen, S. Bashir, J. Liu, Silver-modified $Ba_{1-x}Co_{0.7}Fe_{0.2}Nb_{0.1}O_{3-delta}$ perovskite performing as a cathodic catalyst of intermediate-temperature solid oxide fuel cells, ACS Appl. Mater. Interfaces 12 (2020) 9421–9433.

[40] Q. Fan, S. Zhang, L. Sun, X. Dong, L. Zhang, W. Shan, Z. Zhu, Catalytic oxidation of diesel soot particulates over $Ag/LaCoO_3$ perovskite oxides in air and NO_x, Chin. J. Catal. 37 (2016) 428–435.

[41] T.T.H. Hoang, S. Verma, S. Ma, T.T. Fister, J. Timoshenko, A.I. Frenkel, P.J. A. Kenis, A.A. Gewirth, Nanoporous copper-silver alloys by additive-controlled electrodeposition for the selective electroreduction of CO_2 to ethylene and ethanol, J. Am. Chem. Soc. 140 (2018) 5791–5797.

[42] P. Iyengar, M.J. Kolb, J.R. Pankhurst, F. Calle-Vallejo, R. Buonsanti, Elucidating the facet-dependent selectivity for CO_2 electroreduction to ethanol of Cu–Ag tandem catalysts, ACS Catal. 11 (2021) 4456–4463.

[43] W.J. Dong, C.J. Yoo, J.W. Lim, J.Y. Park, K. Kim, S. Kim, D. Lee, J.-L. Lee, Tailoring electronic structure of bifunctional Cu/Ag layered electrocatalysts for selective CO_2 reduction to CO and CH_4, Nano Energy 78 (2020), 105168.

[44] Y. Chen, W. Yang, S. Gao, C. Sun, Q. Li, Synthesis of Bi_2MoO_6 nanosheets with rich oxygen vacancies by postsynthesis etching treatment for enhanced photocatalytic performance, ACS Appl. Nano Mater. 1 (2018) 3565–3578.

[45] R. Zhong, Q. Wang, L. Du, Y. Pu, S. Ye, M. Gu, Z. Conrad Zhang, L. Huang, Ultrathin polycrystalline Co_3O_4 nanosheets with enriched oxygen vacancies for efficient electrochemical oxygen evolution and 5-hydroxymethylfurfural oxidation, Appl. Surf. Sci. 584 (2022), 152553.

[46] J. Wang, C. Cheng, B. Huang, J. Cao, L. Li, Q. Shao, L. Zhang, X. Huang, Grain-boundary-engineered La_2CuO_4 perovskite nanobamboos for efficient CO_2 reduction reaction, Nano Lett. 21 (2021) 980–987.

[47] W. Luo, X. Nie, M.J. Janik, A. Asthagiri, Facet dependence of CO_2 reduction paths on Cu electrodes, ACS Catal. 6 (2015) 219–229.

[48] J. Dai, Y. Zhu, Y. Chen, X. Wen, M. Long, X. Wu, Z. Hu, D. Guan, X. Wang, C. Zhou, Q. Lin, Y. Sun, S.C. Weng, H. Wang, W. Zhou, Z. Shao, Hydrogen spillover in complex oxide multifunctional sites improves acidic hydrogen evolution electrocatalysis, Nat. Commun. 13 (2022) 1189.

[49] X. Jiang, X. Wang, Z. Liu, Q. Wang, X. Xiao, H. Pan, M. Li, J. Wang, Y. Shao, Z. Peng, Y. Shen, M. Wang, A highly selective tin-copper bimetallic electrocatalyst for the electrochemical reduction of aqueous CO_2 to formate, Appl. Catal. B Environ. 259 (2019), 118040.

[50] B. Liu, X. Yao, Z. Zhang, C. Li, J. Zhang, P. Wang, J. Zhao, Y. Guo, J. Sun, C. Zhao, Synthesis of Cu_2O nanostructures with tunable crystal facets for electrochemical CO_2 reduction to alcohols, ACS Appl. Mater. Interfaces 13 (2021) 39165–39177.